Generation of bulk shear spikes in shallow stratified tidal seas

Hans Burchard *

Leibniz Institute for Baltic Sea Research Warnemünde, Rostock, Germany

Tom P. Rippeth

School of Ocean Sciences, College of Natural Sciences,

Bangor University, United Kingdom

*Corresponding author address: Hans Burchard, Leibniz Institute for Baltic Sea Research Warnemünde, Seestraße 15, D-18119 Rostock, Germany. Visiting at: School of Ocean Sciences, Menai Bridge, College of Natural Sciences, Bangor University, Anglesey LL59 5AB, United Kingdom

E-mail: hans.burchard@io-warnemuende.de

Abstract

Recent fine scale observations of shear and stratification in temperate shelf sea thermoclines show that they are of marginal stability, suggesting that episodes of enhanced shear could potentially lead to shear instability and diapcynal mixing. The bulk shear between the upper and lower boundary layers in seasonally stratified shelf seas shows remarkable variability on tidal, inertial and synoptic timescales which have yet to be explained. In this paper we present observations from the seasonally stratified northern North Sea, at a time when the water column has a distinct two-layer structure. Bulk shear estimates, based on ADCP measurements, show a bulk shear vector which rotates in a clockwise direction at the local inertial period, with episodes of bulk shear spikes which have an approximately twice daily period, and occur in bursts which last for several days. In order to explain this observation we develop a simple two-layer model based on layer averaging of the one-dimensional momentum equation, forced at the surface by wind stress, and damped by (tidally dominated) sea bed friction. The two layers are then linked through an interfacial stress term. The model reproduces the observations, showing that the bulk shear spikes are a result of the alignment of the wind stress, tidal bed stress and (clockwise rotating) bulk shear vectors. Velocity micro-structure measurements are then used to confirm enhanced levels of mixing during a period of bulk shear spikes. A numerical study demonstrates the sensitivity of the spike generation mechanism to the local tidal conditions and phasing and duration of wind events.

1. Introduction

A central part of the current agenda in physical oceanography of continental shelf seas is the identification and parameterisation of processes which drive vertical mixing across the seasonal thermocline. The seasonal thermocline acts as an important physical barrier separating the sunlit surface layers from the dark nutrient rich deep water. The mixing of material across the seasonal thermocline therefore represents a key biogeochemical pathway (Sharples et al. (2001)).

Coincident high resolution measurements of shear and stratification (e.g. van Haren et al. (1999); MacKinnon and Gregg (2005); Rippeth et al. (2005); Rippeth (2005)) for a range of temperate seasonally stratified shelf seas show that the thermocline is in a state of marginal stability (gradient Richardson number, $R_i \approx 1$), implying that the addition of extra shear could potentially reduce R_i sufficiently to trigger shear instability, thus transferring energy to thermocline turbulence and resulting in vertical mixing. Whilst flow in continental shelf seas tends to be dominated by the tides (e.g. Rippeth et al. (2005)), currents also arise because of wind-driven slab motion of the surface layer. These near-inertial oscillations are the response to abrupt changes in wind forcing. They have long been recognised as energetic features throughout the ocean (e.g. Pollard (1980), Itsweire et al. (1989)) and continental shelf seas (Chant (2001); Chen et al. (1996)). Indeed, they are observed to account for a significant proportion of the observed current variance in some tidally energetic coastal seas (e.g. Shearman (2005)). Layers of strong shear tend to coincide with layers of strong stratification and cover extended areas with strong vertical veering but little horizontal variability in shear direction (Itsweire et al. (1989)). The latter authors found for Monterey Bay that the mean shear direction within the shear layer rotated at the local inertial frequency.

In coastal seas the presence of a coastline produces a barotropic response resulting in a 180°

phase shift across the thermocline (Krauß (1979), Craig (1989), Rippeth et al. (2002); Simpson et al. (2002); Shearman (2005)), resulting in enhanced shear and a potentially significant source of mixing in shelf seas. Estimates of the rate at which near-inertial oscillations are damped (Sherwin (1987)) are suggestively consistent with TKE dissipation rates observed in the seasonal thermocline (Rippeth (2005)).

In this paper we develop a simple analytical model to investigate a mechanism for the generation of periods of enhanced shear across the seasonal thermocline, which mainly result from interaction between shear itself and surface wind stress. In the first section of the paper we present observations of wind and bulk shear from the seasonally stratified northern North Sea, for a period when the water column exhibited a two-layer structure (section 2). We then derive a theory for bulk shear generation in two-layer flows (section 3) which is then applied to the observations from the northern North Sea (section 4.a). In section 4.b of the paper the correlation between bulk shear, wind stress and observed mixing estimates, based on micro-structure measurements, is investigated. Finally a numerical sensitivity study is undertaken (section 5) and conclusions drawn (section 6).

Note that for simplicity the sense of rotation is always related to the northern hemisphere. Thus clockwise means anti-cyclonic and anti-clockwise means cyclonic sense of rotation.

2. Observations

During the EU-funded PROVESS (PROcesses of VErtical Stratification in Shelf seas) project, intense water column measurements were carried out in the Northern North Sea (NNS) at 59°20'N and 1°E, with a water depth of 110 m. At the central station A (see figure 1 for the

location) over the period 8 September to 2 November 1998, current velocities were observed using a bottom mounted 150 kHz broad band RD Instruments Acoustic Doppler Current Profiler (ADCP) returning 10-minute averages between 11 m and 87 m below the sea surface, with a bin size of 4 m (for details, see Knight et al. (2002)). These observations were accompanied by CTD (Conductivity-Temperature-Depth) casts and thermistor chain observations at adjacent locations for measurements of the stratification, as well as velocity micro-structure profiles (Prandke et al. (2000)) from which the rate of turbulent dissipation (ε) and thus vertical mixing rate is estimated (Burchard et al. (2002)). Meteorological parameters have been obtained from the Frigg oil rig at 59°54'N and 2°6'E (about 48 nm north-east of the central station A, see figure 1. These data have been used to calculate surface stresses using bulk formulae (Kondo (1975)).

Tides are predominantly semi-diurnal, rotating in a clockwise sense, with M_2 and S_2 amplitudes of 0.20 $\mathrm{m\,s^{-1}}$ and 0.07 $\mathrm{m\,s^{-1}}$, respectively (Knight et al. (2002)) and the ellipticity of the M_2 tide is about 1:3 (Davies et al. (1997)), and the major axis oriented in meridional direction.

A characteristic feature which Knight et al. (2002) analysed from the PROVESS-NNS current velocity data is that near-inertial oscillations which clearly dominate the signal in the surface and the bottom mixed layer are absent in the vertically averaged current velocities, due to a 180° phase shift between the two layers. Knight et al. (2002) could partially explain this feature by applying the theory of Craig (1989) as due to the presence of an adjacent coast which set up a barotropic pressure gradient accelerating the water column in the opposite direction of the wind-driven Ekman transport.

The observations of temperature and salinity at the PROVESS-NNS site showed a distinct three-layer structure of the water column at the beginning of the measurements in early Septem-

ber, with a bottom boundary layer and a surface boundary layer being separated by a 30 - 40 m thick diffuse thermocline. However, the erosion of this intermediate layer by surface cooling resulted in the development of a clear two-layer structure with surface and bottom boundary layers separated by a stratified region of less than 20 m thickness which persisted until the end of the observations.

A 10-day period of the observations, between 16 October (day 288) and 26 October 1998 (day 298) is selected to be the focus of this study because the water column has a clear two-layer structure at this time (figure 2).

Figure 3 shows the observed 10 m wind, the bulk shear squared and the shear direction. Here the bulk shear is calculated by first identifying the depth of strongest vertical stratification (typically about mid-depth), then averaging the observed current velocities over the resulting surface and bottom layers, and finally dividing the difference of the two velocities by half of the water depth. The shear direction is the direction of the resulting shear vector with respect to North (0°) in a clockwise rotating sense. The period of interest is characterised by typically strong but changeable winds of up to 20 $\mathrm{m\,s^{-1}}$ velocity. In contrast to that, the observed bulk shear shows distinct peaks twice daily. Periods of an enhanced background bulk shear are observed during days 289 and 290 and again between days 294 and 297. In contrast the bulk shear is small between days 291 and 293, despite the occasionally strong winds at this time.

It is thus concluded that the magnitude of the individual shear spikes is not directly correlated to the magnitude or direction of the wind. An analysis of the shear direction shows that it rotates in a clockwise sense at the local inertial period of 13.91 h, with occasional deviations from the inertial period, see the bottom panel in figure 3. This observation is in agreement with the findings of Itsweire et al. (1989).

The focus of the present study is to explain the development of the observed shear spikes as function of wind and tide. This is achieved using a simple two-layer theory which will be developed in the next section of the paper.

3. Theory

The theory for bulk shear dynamics is based on the one-dimensional momentum equations on the rotating Earth,

$$\begin{aligned} \partial_t u - \partial_z \tau^x - fv &= -g\partial_x \eta, \\ \partial_t v - \partial_z \tau^y + fu &= -g\partial_y \eta, \end{aligned} \tag{1}$$

with the eastward and northward velocity components u and v, respectively, the shear stress components normalised by density, τ^x and τ^y, the Coriolis parameter f, the gravitational acceleration g and the surface elevation slopes, $\partial_x \eta$ and $\partial_y \eta$, the latter two terms providing a prescribed barotropic pressure gradient forcing. Horizontal density gradients, lateral advection and mixing and variations in water depth h are neglected as well as shear generated by internal waves, assuming a distance from the nearest coast or frontal feature of at least a few internal Rossby radii.

Definition of an arbitrary intermediate depth z_i with $-h < z_i < 0$ and upper layer and lower layer thicknesses $h_s = -z_i$ and $h_b = z_i + h$, respectively, leads to the definition of upper and layer layer velocity components

$$\begin{aligned} u_s &= \frac{1}{h_s}\int_{z_i}^{0} u(z)\,\mathrm{d}z, \quad u_b = \frac{1}{h_b}\int_{-h}^{z_i} u(z)\,\mathrm{d}z, \\ v_s &= \frac{1}{h_s}\int_{z_i}^{0} v(z)\,\mathrm{d}z, \quad v_b = \frac{1}{h_b}\int_{-h}^{z_i} v(z)\,\mathrm{d}z, \end{aligned} \tag{2}$$

and depth-mean velocity components

$$u_m = \frac{1}{h}\int_{-h}^{0} u(z)\,\mathrm{d}z, \quad v_m = \frac{1}{h}\int_{-h}^{0} v(z)\,\mathrm{d}z, \tag{3}$$

such that

$$u_s h_s + u_b h_b = u_m h, \quad v_s h_s + v_b h_b = v_m h. \tag{4}$$

Integrating the momentum equations (1) over the upper and the lower layer, respectively, and defining the surface stress as $\tau_s^x = \tau^x(0), \tau_s^y = \tau^y(0)$, the interfacial stress as $\tau_i^x = \tau^x(z_i), \tau_i^y = \tau^y(z_i)$, and the bottom stress as $\tau_b^x = \tau^x(-h), \tau_b^y = \tau^y(-h)$, dynamical equations for the upper and lower layer velocity components are obtained:

$$\begin{aligned} \partial_t u_s - \frac{1}{h_s}\tau_s^x + \frac{1}{h_s}\tau_i^x - f v_s &= -g\partial_x \eta, \\ \partial_t u_b - \frac{1}{h_b}\tau_i^x + \frac{1}{h_b}\tau_b^x - f v_b &= -g\partial_x \eta, \end{aligned} \tag{5}$$

and

$$\begin{aligned} \partial_t v_s - \frac{1}{h_s}\tau_s^y + \frac{1}{h_s}\tau_i^y + f u_s &= -g\partial_y \eta, \\ \partial_t v_b - \frac{1}{h_b}\tau_i^y + \frac{1}{h_b}\tau_b^y + f u_b &= -g\partial_y \eta. \end{aligned} \tag{6}$$

After defining the bulk shear vector components as

$$S_u = \frac{u_s - u_b}{\frac{1}{2}h}, \quad S_v = \frac{v_s - v_b}{\frac{1}{2}h}, \tag{7}$$

equations for the bulk shear may be derived from (5) and (6):

$$\begin{aligned} \partial_t S_u - \frac{2}{h_s h}\tau_s^x + \frac{2}{h_s h_b}\tau_i^x - \frac{2}{h_b h}\tau_b^x - f S_v &= 0, \\ \partial_t S_v - \frac{2}{h_s h}\tau_s^y + \frac{2}{h_s h_b}\tau_i^y - \frac{2}{h_b h}\tau_b^y + f S_u &= 0. \end{aligned} \tag{8}$$

After parameterising the interfacial shear stress by means of a quadratic friction law as

$$\begin{aligned} \tau_i^x &= c_i(u_s - u_b)\left((u_s - u_b)^2 + (v_s - v_b)^2\right)^{1/2} = \frac{1}{4}h^2 c_i S_u S, \\ \tau_i^y &= c_i(v_s - v_b)\left((u_s - u_b)^2 + (v_s - v_b)^2\right)^{1/2} = \frac{1}{4}h^2 c_i S_v S, \end{aligned} \tag{9}$$

with the interfacial drag coefficient c_i, and the bulk shear squared,

$$S^2 = S_u^2 + S_v^2, \tag{10}$$

multiplication the first equation in (8) with $2S_u$ and the second equation in (8) with $2S_v$ and adding the two, a dynamical equation for the bulk shear squared S^2 is obtained:

$$\begin{aligned} \partial_t S^2 &= \frac{4}{h}\vec{S}\cdot\left(\frac{\vec{\tau}_s}{h_s}+\frac{\vec{\tau}_b}{h_b}\right) &- c_i\frac{h^2}{h_s h_b}S^3 \\ &= P\left(S^2\right) &- D_i\left(S^2\right), \end{aligned} \tag{11}$$

with the bulk shear vector, $\vec{S}=(S_u,S_v)$, the surface shear stress vector, $\vec{\tau}_s=(\tau_s^x,\tau_s^y)$ and the bottom shear stress vector, $\vec{\tau}_b=(\tau_b^x,\tau_b^y)$. Equation (11) shows that bulk shear is generated or reduced by the scalar product of bulk shear and the weighted sum of surface and bottom stress (first term of right hand side), $P\left(S^2\right)=P_s\left(S^2\right)+P_b\left(S^2\right)$, and dissipated by interfacial friction (second term on right hand side), $D_i\left(S^2\right)$. The maximum bulk shear production rate for given absolute values of surface and bottom shear stress is obtained for a perfect alignment of the three vectors, surface shear stress, bottom shear stress and bulk shear. Although the barotropic pressure gradient does not explicitly appear in eq. (11), it still has an indirect effect by changing the bottom layer velocity and thus the bottom friction. With this a potential 180 ° phase shift as suggested by the Craig (1989) condition is implicitly included in the present theory.

To highlight the role of tidal forcing, a parameterisation for the bottom stress is used:

$$\begin{aligned} \tau_b^x &= c_d u_b\left(u_b^2+v_b^2\right)^{1/2} = c_d\left(u_m-\frac{1}{2}h_s S_u\right)\left(u_b^2+v_b^2\right)^{1/2}, \\ \tau_b^y &= c_d v_b\left(u_b^2+v_b^2\right)^{1/2} = c_d\left(v_m-\frac{1}{2}h_s S_v\right)\left(u_b^2+v_b^2\right)^{1/2}, \end{aligned} \tag{12}$$

where

$$u_b = u_m-\frac{1}{2}h_s S_u, \quad v_b = v_m-\frac{1}{2}h_s S_v \tag{13}$$

has been used as derived from (4). In (12), c_d is the bottom drag coefficient with respect to the bottom layer thickness h_b.

With (12), the dynamical equation (11) for the bulk shear squared can be reformulated:

$$
\begin{aligned}
\partial_t S^2 &= \frac{4}{h}\,\vec{S}\cdot\left(\frac{\vec{\tau}_s}{h_s}+\frac{c_d\vec{V}_m\left|\vec{V}_b\right|}{h_b}\right)-c_i\frac{h^2}{h_s h_b}S^3-c_d\frac{2h_s}{h_b h}S^2\left|\vec{V}_b\right| \\
&= P_s\left(S^2\right)+P_m\left(S^2\right)-D_i\left(S^2\right)-D_b\left(S^2\right),
\end{aligned}
\tag{14}
$$

with the depth-mean velocity vector, $\vec{V}_m=(u_m,v_m)$ and the lower layer velocity vector, $\vec{V}_b=(u_b,v_b)$. In (14) the production of bulk shear is now formulated as the scalar product of bulk shear with the weighted sum of the surface shear stress and the depth-mean velocity, $P_s\left(S^2\right)$ and $P_m\left(S^2\right)$, respectively. It should be noted that both, $P_s\left(S^2\right)$ and $P_m\left(S^2\right)$, may increase or decrease S^2. The bed stress appears here as an additional sink of bulk shear, $D_b\left(S^2\right)$, such that $P_m\left(S^2\right)-D_b\left(S^2\right)=P_b\left(S^2\right)$.

Although the direct effect of Earth rotation on bulk shear squared is eliminated in equations (11) and (14), the bulk shear vector $\vec{S}$ is subject to Earth rotation, see equation (8). In the northern hemisphere, $\vec{S}$ has therefore the tendency to rotate in clockwise direction with a period $2\pi/f$ (the local inertial period).

The formulation of the bottom stress by means of the barotropic velocity, (u_m,v_m), see equation (12), gives another interesting interpretation of the bulk shear equations (8):

$$
\begin{aligned}
\partial_t S_u - fS_v &= \frac{2}{h_s h}\tau_s^x + c_d\frac{2}{h_b h}|\vec{V}_b|u_m - \left(c_i\frac{h^2}{2h_s h_b}S + c_d\frac{h_s}{h_b h}|\vec{V}_b|\right)S_u, \\
\partial_t S_v + fS_u &= \frac{2}{h_s h}\tau_s^y + c_d\frac{2}{h_b h}|\vec{V}_b|v_m - \left(c_i\frac{h^2}{2h_s h_b}S + c_d\frac{h_s}{h_b h}|\vec{V}_b|\right)S_v.
\end{aligned}
\tag{15}
$$

With this, the bulk shear can be interpreted as a pendulum in a rotating reference frame, forced by wind and tide (first two terms on right hand side) and damped by interfacial and bottom friction (last term on right hand side).

For a circular tide with frequency ω and zero interfacial friction ($c_i=0$) and zero surface stress ($\vec{\tau}_s=\vec{0}$), the bulk shear equations (15) can be simplified to

$$\partial_t S_u - f S_v = a \cos \omega t - b S_u,$$
$$\partial_t S_v + f S_u = a \sin \omega t - b S_v, \tag{16}$$

with

$$a = c_d \frac{2}{h_b h} |\vec{V_b}| A_t; \quad b = c_d \frac{h_s}{h_b h} |\vec{V_b}|, \tag{17}$$

where A_t denotes the tidal velocity amplitude. For circular tides, $|\vec{V_b}|$ can be assumed to be a constant with $|\vec{V_b}| \approx A_t$. For $\omega > 0$, tides are rotating in an anti-clockwise sense, and for $\omega < 0$ rotation is in a clockwise sense.

An analytical solution to (16) is found by defining the complex shear $S^c = S_u + iS_v$ with $i = \sqrt{-1}$, and transforming (16) into a dynamical equation for S^c by multiplying the second equation in (16) with i and adding the two equations:

$$\partial_t S^c + i f S^c = a \exp(i\omega t) - b S^c. \tag{18}$$

With the solution of the resulting equation,

$$S^c = A \exp(i\omega t) = A(\cos \omega t + i \sin \omega t), \tag{19}$$

the shear amplitude is analytically obtained as the absolute value of A:

$$|A| = \frac{a}{\left((\omega + f)^2 + b^2\right)^{1/2}}. \tag{20}$$

Thus for clockwise tides, shear is strongly enhanced whilst it is suppressed by anti-clockwise tides. This result is consistent with theoretical analysis (Prandle (1982)) which predicts that tides rotating in a clockwise sense create considerably more shear than tides rotating in an anti-clockwise sense.

With this, shear rotating at tidal frequency and amplitude is the background state for zero wind stress. Wind events will generate shear rotating in a clockwise sense at inertial frequency, overlaying this background rotation.

4. Analysis of field data

a. Impact of wind stress on shear spikes

A comparison of wind stress with bulk shear does not reveal any clear relationship between these two quantities, see the discussion (section 2). For example, peaks in the wind stress at $d = 293.0$ and $d = 296.8$ do not coincide with maxima in bulk shear and bulk shear maxima at $d = 290.0$ and $d = 295.7$ are not associated with distinct wind stress maxima, see figure 4.

To reproduce the bulk shear production term in equation (11), $P\left(S^2\right)$, the bed stress, $\vec{\tau}_b$, is estimated from the current measurements. Using a bed roughness length of $z_0^b = 0.001$ m for this site (Bolding et al. (2002)), a bed friction coefficient of $c_d = 0.0015$ is derived from the law of the wall, based on the average bottom layer thickness of 55 m. This leads to a bed stress estimate which is significantly smaller than the wind stress for the period of interest, such that the wind stress predominantly drives the bulk shear (figure 5a).

With this bottom drag coefficient, the curves for the time derivative of the observed bulk shear squared, $\partial_t S^2$, and the production of bulk shear squared, $P\left(S^2\right)$, agree very well (figure 4c), thus providing clear validation of equation (11) as a description of the dynamics of this two-layer flow.

In order to maximise $P\left(S^2\right)$, the product of the surface stress and the bulk shear must be large with the two vectors well aligned. In figure 4 all alignments of bulk shear and wind

direction preceding a shear spike with $S^2 > 2 \cdot 10^{-5}$ s^{-2} are indicated with a circle. Nine such shear spikes are identified for the 10-day period under consideration. The instants of alignment coincide with distinct maxima of $P\left(S^2\right)$ and thus with the maxima in $\partial_t S^2$. Therefore these alignments also mark the steepest ascent to the maxima of S^2, typically occurring a quarter of an inertial period before the bulk shear maxima, which coincide with zero values of $P\left(S^2\right)$. The two largest shear spikes occur at days 290.0 and 295.7, due to the coincidence of high shear stresses >0.4 N m^{-2} and shear squared values $>2 \cdot 10^{-5}$ s^{-2} with the alignment of wind and shear directions. In contrast the wind stress maximum on day 293.0 coincided with a small shear squared value, resulting in only a moderate subsequent bulk shear peak.

The role of the bed stress in the dynamics of bulk shear is shown in figure 5. From the second panel it is obvious that shear and bed stress are generally out of phase by about 180°, which is pronounced during days 295 and 296. The explanation for this is given by the 180° phase shift between the bottom and surface layers. With relatively weak tides this results in a positive east component of bulk shear coinciding with negative near-bed velocity and thus negative bed stress in the eastern direction, and vice versa. Consequently the bed stress contribution to the bulk shear is predominantly negative here, specifically during days 295 and 296 (figure 5c). For example, on day 293.0 the bed stress peaks at a phase shift of 180° to the bulk shear, thus reducing the impact of the strongest wind stress peak on the generation of bulk shear.

To discriminate between the barotropic (mainly tidal) and bed stress contributions to the bulk shear, the mean flow production, $P_m\left(S^2\right)$, and the bed friction related dissipation, $D_b\left(S^2\right)$, are calculated according to equation (14), see figure 6a. Clearly the tidal contribution may be positive during periods of up to two days (e.g., days 288 and 289). This is because the tide is rotating in a clockwise sense, and is in phase with the shear over longer periods (figure 6b). Part

of the positive tidal contribution is always counter-balanced by the bed friction.

b. Impact of shear spikes on isopycnal mixing

A major consequence of increased bulk shear may be shear instability (as the gradient Richardson number R_i is reduced) resulting in increased diapycnal mixing. The reduction of R_i is however directly related to local shear across the thermocline, and not to the bulk shear.

In order to connect increased bulk shear with enhanced diapycnal mixing across the thermocline, bulk shear is compared to shear across the thermocline (the position of which is derived from thermistor chain data), see figure 7. Naturally, the local shear, S_i, calculated as the shear across the two 4 m ADCP bins located at the maximum stratification, is much larger than the bulk shear, but high local shears seem to be largely induced by high bulk shears.

With the aid of the local shear and assumptions about the interfacial eddy viscosity, K_m, the interfacial drag coefficient may be roughly estimated:

$$\tau_i = c_i \frac{h^2}{4} S^2 = K_m S_i \quad \Rightarrow \quad c_i = K_m \frac{4 S_i}{h^2 S^2}. \tag{21}$$

Taking a typical value of $K_m = 10^{-5}\mathrm{m}^2\mathrm{s}^{-1}$, see table 1, the interfacial drag coefficient resulted in $c_i \approx 4 \cdot 10^{-6}$. A comparison between the bulk shear loss due to interfacial friction, $D_i\left(S^2\right)$, calculated with this value of c_i , with the bed friction loss, $D_b\left(S^2\right)$, shows that interfacial friction is dynamically negligible here.

To investigate the relationship between the generation of turbulence and consequent diapycnal mixing, and the surface wind stress and bulk shear, time series of bulk shear and wind stress are shown together with estimates for the dissipation rate and eddy diffusivity from micro-structure data, see figure 8. Each micro-structure data point represents an average of all data

within the thermocline with $N^2 > 5 \cdot 10^{-4}\mathrm{s}^{-2}$ (where N is the buoyancy frequency) averaged over one burst (which corresponds to approx. 5 profiles taken over a period of about 30 minutes).

The dissipation rate and stratification data are then combined to obtain estimates for the eddy diffusivity K_ρ, using the local equilibrium assumption for the turbulent kinetic energy equation, i.e. the assumption of a balance between shear production, buoyancy production and dissipation, resulting in

$$K_\rho = \Gamma \frac{\varepsilon}{N^2}, \tag{22}$$

with the mixing efficiency $\Gamma = -B/\varepsilon$ where B is the buoyancy production (negative for stable stratification). Osborn (1980) estimated $\Gamma = 0.2$ to be an upper limit for the mixing efficiency in stably stratified flow, a value which is used here for estimating K_ρ using (22).

Although there is considerable scatter (Figure 8) the average values of dissipation rate and eddy diffusivity are clearly higher during the high shear phase, day 294.0, than during the low shear phase, after day 290.0.

A more rigorous comparison is achieved by comparing two 2.5 day periods of data, days 290.0 - 292.5 and days 294.0 - 296.5. The wind strength is similar during both periods, however during the first period there is relatively small bulk shear and during the second period there is relatively high bulk shear. Since near surface dissipation rates scale with the cube of the surface friction velocity (according to the law of the wall) and the dissipation of bulk shear squared is proportional to the cube of the bulk shear, averages of S^3 and $(\tau^s)^{3/2}$ are calculated for comparison (table 1). For both periods, average dissipation rate and eddy diffusivity are calculated. The results show that the eddy diffusivity correlates more strongly with the bulk shear than with the wind stress, with a threefold increase in S^3 during the second period when

compared to the first, coinciding with a five fold increase in the value of K_ρ, despite the fact that the average $(\tau^s)^{3/2}$ is smaller during the second period (figure 8). The average dissipation rate also increases by about a factor of 2.5 between the first and second periods. The bootstrap method has been used to show the significance of these results (table 1).

The comparison shows clearly that bulk shear has a stronger impact on diapycnal mixing than surface wind stress.

5. Sensitivity studies

In section 4a we have shown that the bulk shear is highly sensitive to the duration of the wind events, and the phasing of the wind and bulk shear directions.

To better understand the impact of the wind on the shear spike generation, a systematic sensitivity analysis, using the simple two-layer model, is carried out. The numerical model is a discretisation of equations (5) and (6), with the surface slopes calculated in such a way, that a prescribed (tidal) depth-mean flow results. This is obtained numerically by adding (for each time step) a constant value to the calculated velocity vectors in the upper and the lower layer in such a way that the prescribed depth-mean velocity vector is obtained (see Burchard (1999)). The interfacial drag coefficient has been set to $c_i = 10^{-5}$ and the bottom drag coefficient to $c_d = 1.5 \cdot 10^{-3}$. The time step is chosen such that each tidal period is resolved with 1000 time steps, short enough to exclude significant discretisation errors.

For comparison with the field data, the water depth (110 m) and latitude (59°20'N) of station A are used, with the interface between the two layers set at mid-depth. A tide with a tidal amplitude of $A_t = 0.3$ m s^{-1} for a recti-linear tide and of $A_t = 0.3/\sqrt{2}$ m s^{-1} for circular

tides has been prescribed, giving the same average tidal kinetic energy for both cases. All model simulations have been integrated during 50 periods of the M_2 tide (period $T = 44714$ s), of which the last 10 periods are then analysed. Periodic wind events from west have been prescribed by means of a Gaussian wind evolution with a maximum wind speed of $W_{\max} = 20$ m s^{-1}:

$$W_x = \max_i \left\{ W_{\max} \exp\left(-\frac{(t - t_i)^2}{\left(\frac{d}{2}\right)^2} \right) \right\}, \tag{23}$$

with the duration of the wind event, d, and the wind peak instants $t_i/T =$ 5.0, 15.0, 25.0, 35.0, and 45.0.

From these given wind speeds, surface stresses have been calculated using a quadratic drag law with a drag coefficient of 10^{-3}.

A total number of 24 simulations have been carried out, with variations in

- tidal ellipticity (clockwise circular; recti-linear east-west; anti-clockwise circular),
- initial phase of tide relative to wind (0°; 90°; 180°; 270°),
- duration of wind (one tidal period: $d = T$; three tidal periods: $d = 3T$).

To investigate the impact of the phase of the wind in detail, the model is first run with a clockwise circular tidal forcing with a wind event duration of $d = T$ and initial tidal phase shifts of 270° and 90° (figures 9 and 10). For the 270° initial phase shift, the bulk shear squared peaks at a value of $1.6 \cdot 10^{-5}$s^{-2}, whilst for the 90° initial phase shift, bulk shear is close to a minimum value during the wind peak with values $< 5 \cdot 10^{-6}$s^{-2}. The strong shear peak in the former case is because the wind direction (constantly 90°) and shear direction are almost aligned during the maximum wind stress, leading to a large peak in shear production P_s at $t/T = 5$. In

contrast for the second period, the angle between the wind and shear direction remains close to 90° during the wind peak, resulting in a small values of P_s. An interesting feature is that the shear remains in a southerly direction throughout the wind event as a result of the westerly wind blocking the southerly, clockwise rotating shear from further rotating towards the west. For both initial phase shifts, shear production due to depth-mean velocity, P_m, is small, slightly positive when the angle between shear and the depth-mean velocity is $<$90°, and slightly negative when this angle is $>$90°. In both cases, dissipation due to bed friction, D_b is dominated by, and largely proportional to, S^2, with the interfacial friction, D_i, negligible.

Figures 11 and 12 show time series of bulk shear square, S^2 (thin lines) and its shear production, P_s (bold lines) for all 24 simulations outlined above. A number of general observations can be made here:

- For short and intense wind events the phasing with the bulk shear direction is critical in determining their impact on the intensity of the shear. Short wind peaks may either strongly enhance, or significantly reduce the bulk shear. The latter may be compared to the relatively small impact of the wind peaks during the observational period days 293.0 and 297.6, see figure 4.

- For wind events of a duration significantly longer than the inertial period, the relative phase to the shear direction does not play such an important role. Longer wind events result in a number of subsequent shear peaks each occurring approximately one inertial period after the preceding peak. This may be compared to the series of shear peaks occurring during the extended wind event between days 288.5 and 290.3 (figure 4).

- For anti-clockwise tides, the effect of wind events on the bulk shear is significantly weaker than for clockwise tides. Inserting the parameters used for the present study into the

analytical solution (20) for the shear amplitude (neglecting wind stress and interfacial friction), $|A|^2 = 2.1 \cdot 10^{-6}\text{s}^{-2}$ results for the clockwise tide, and $|A|^2 = 7.0 \cdot 10^{-9}\text{s}^{-2}$ results for the anti-clockwise tide. These values are almost identical to those shear square values which result for the clockwise and anti-clockwise numerical experiments with the extended wind event, when the effect of the wind has ceased, see figure 12.

- The angle between wind and shear directions thus plays a far less important role for anti-clockwise rotating tides than it does for clockwise rotating tides.

6. Discussion and conclusions

Recent fine scale observations of shear and stratification in temperate shelf sea thermoclines show that they are of marginal stability suggesting that episodes of enhanced shear could potentially lead to shear instability and diapcynal mixing (van Haren et al. (1999); MacKinnon and Gregg (2005); Rippeth et al. (2005); Rippeth (2005)). Here we present observations from the northern North Sea which show that the bulk shear vector rotates in a clockwise direction at the local inertial frequency, with periods of enhanced bulk shear taking the form of shear spikes which are separated by approximately one inertial period, and which occur in bursts lasting several days. Similar observations of the bulk shear are reported for the seasonally stratified western Irish Sea (Rippeth et al. (2008)) and the Celtic Sea (Palmer et al. (2008)).

A two-layer analytical model has been derived to explain the observed characteristics of the bulk shear. The model results show that the shear ‘spikes’ arise because of the alignment of the surface wind stress, bulk shear and bed stress vectors, thus indicating the sensitivity of the system to both the phase and direction of the wind. The results also highlight the important role

of the sense of rotation of the tide in determining the level of diapcynal shear and mixing, thus confirming the theoretical result of Prandle (1982) and the observations of Simpson and Tinker (2008) in the bottom boundary layer.

The results will present particular problems for numerical models due to the requirement of the alignment of the 'local' wind vector with the bulk shear direction, the phase of which will have been set by some previous event. These problems are compounded by the further result that short wind events have the potential to generate stronger shear spikes than longer wind events, which typically generate a sequence of shear spikes.

Application of the model to other areas requires velocity and density profiles together with local wind conditions. Because the interfacial stresses are negligible compared to typical bottom and surface stresses, the theory can easily be extended to three layers, in order to accommodate a diffuse thermocline. The model does not, however, include shear associated with long internal waves, which may form an important source of shear in some areas.

Acknowledgments.

The work of Hans Burchard has been supported by a Kirby Laing Fellowship at the School of Ocean Sciences of the University of Wales in Bangor and the EU-funded project ECOOP (European COastal-shelf sea OPerational monitoring and forecasting system, Contract No. 36355). Additional work was carried out under NERC grant NE/F002432. All field data have been obtained during the EU-funded PROVESS (PROcesses of VErtical Stratification in Shelf seas) project. The authors are grateful to Adolf Stips (Ispra, Italy) for providing the MST microstructure profiler data. Comments on the manuscript by Hans Ulrich Lass (Warnemünde, Germany) and two anonymous referees were highly appreciated.

References

Bolding, K., H. Burchard, T. Pohlmann, and A. Stips, 2002: Turbulent mixing in the Northern North Sea: a numerical model study. *Cont. Shelf Res.*, **22**, 2707–2724.

Burchard, H., 1999: Recalculation of surface slopes as forcing for numerical water column models of tidal flow. *App. Math. Modelling*, **23**, 737–755.

Burchard, H., K. Bolding, T. P. Rippeth, A. Stips, J. H. Simpson, and J. Sündermann, 2002: Microstructure of turbulence in the Northern North Sea: A comparative study of observations and model simulations. *J. Sea Res.*, **47**, 223–238.

Chant, R. J., 2001: Evolution of near-inertial waves during an upwelling event on the New Jersey inner shelf. *J. Phys. Oceanogr.*, **31**, 746–764.

Chen, C., R. O. Reid, and W. D. Nowlin, 1996: Near-inertial oscillations over the Texas-Louisiana shelf. *J. Geophys. Res.*, **101**, 3509–3524.

Craig, P. D., 1989: A model for diurnally forced vertical current structure near 30° latitude. *Cont. Shelf Res.*, **9**, 965–980.

Davies, A. M., S. C. M. Kwong, and R. A. Flather, 1997: Formulation of a variable-function three-dimensional model, with applications to the M_2 and M_4 tide on the North-West European Continental Shelf. *Cont. Shelf Res.*, **17**, 165–204.

Itsweire, E. C., T. R. Osborn, and T. P. Stanton, 1989: Horizontal distribution and characteristics of shear layers in the seasonal thermocline. *J. Phys. Oceanogr.*, **19**, 302–320.

Knight, P. J., M. J. Howarth, and T. P. Rippeth, 2002: Inertial currents in the Northern North Sea. *J. Sea Res.*, **47**, 269–284.

Kondo, J., 1975: Air-sea bulk transfer coefficients in diabatic conditions. *Bound. Layer Meteor.*, **9**, 91–112.

Krauß, W., 1979: Inertial waves in an infinite channel of rectangular cross section. *Dt. Hydrogr. Z.*, **32**, 249–266.

MacKinnon, J. and M. C. Gregg, 2005: Near-inertial waves on the New England shelf: The role of evolving stratification, turbulent dissipation, and bottom drag. *J. Phys. Oceanogr.*, **35**, 2408–2424.

Osborn, T. R., 1980: Estimates of the local rate of vertical diffusion from dissipation measurements. *J. Phys. Oceanogr.*, **10**, 83–89.

Palmer, M. R., T. P. Rippeth, and J. H. Simpson, 2008: An investigation of internal mixing in a seasonally stratified shelf sea. *J. Geophys. Res.*, accepted for publication.

Pollard, R. T., 1980: Properties of near-surface inertial oscillations. *J. Phys. Oceanogr.*, **10**, 385–398.

Prandke, H., K. Holtsch, and A. Stips, 2000: MITEC technology development: The microstructure/turbulence measuring system mss. Tech. Rep. EUR 19733 EN, European Commission, Joint Research Centre, Ispra, Italy.

Prandle, D., 1982: The vertical structure of tidal currents. *Geophysical and Astrophysical Fluid Dynamics*, **22**, 29–49.

Rippeth, T. P., 2005: Mixing in seasonally stratified shelf seas: a shifting paradigm. *Phil. Trans. R. Soc. Lond. A*, **363**, 2837–2854.

Rippeth, T. P., M. R. Palmer, J. H. Simpson, and N. R. Fisher, 2005: Thermocline mixing in summer stratified continental shelf seas. *Geophys. Res. Lett.*, **32**, L05 602, doi:10.1029/2004GL022 104.

Rippeth, T. P., J. H. Simpson, R. J. Player, and M. C. Garcia, 2002: Current oscillations in the inertial-diurnal band on the Catalonian shelf in spring. *Cont. Shelf Res.*, **22**, 247–265.

Rippeth, T. P., J. H. Simpson, E. Williams, and M. E. Inall, 2003: Measurement of the rates of production and dissipation of turbulent kinetic energy in an energetic tidal flow: Red Wharf Bay revisited. *J. Phys. Oceanogr.*, **33**, 1889–1901.

Rippeth, T. P., P. J. Wiles, M. R. Palmer, J. H. Simpson, J. Sharples, and J. Tweddle, 2008: A wind driven nutrient pump. *Cont. Shelf Res.*, submitted.

Sharples, J., C. M. Moore, T. P. Rippeth, P. M. Holligan, D. J. Hydes, N. R. Fisher, and J. H. Simpson, 2001: Phytoplankton distribution and survival in the thermocline. *Limnol. Oceanogr.*, **46**, 486–496.

Shearman, R. K., 2005: Observations of near-inertial current variability on the New England shelf. *J. Geophys. Res.*, **110**, C02 012, doi:10.1029/2004JC002 341.

Sherwin, T. J., 1987: Inertial oscillations in the Irish Sea. *Cont. Shelf Res.*, **7**, 191–213.

Simpson, J. H., P. Hyder, T. P. Rippeth, and I. M. Lucas, 2002: Forced oscillations near the critical latitude for diurnal-inertial resonance. *J. Phys. Oceanogr.*, **32**, 177–187.

Simpson, J. H. and J. P. Tinker, 2008: A test of the influence of tidal stream polarity on the structure of turbulent dissipation. *Cont. Shelf Res.*, in print.

van Haren, H., L. Maas, J. T. F. Zimmerman, and H. R. H. Malschaert, 1999: Strong inertial currents and marginal internal wave stability in the central North Sea. *Geophys. Res. Lett.*, **26**, 2993–2996.

List of Figures

1 Location of the PROVESS station A in the Northern North Sea (at 59°20'N and 1°E, marked by a star) at a water depth of 110 m. The location of the Frigg oil rig where meteorological parameters have been observed is marked by a circle (at 59°54'N and 2°6'E). Contour lines and shading show the water depth, the contour interval is 50 m. 27

2 Observed profiles of potential temperature, salinity, potential density and buoyancy frequency squared at the beginning (16 October 1998, 7:03 h) and one day before the end (24 October 1998, 17:04 h) of the investigated 10-day period. . 28

3 Observations of wind and bulk shear vector in the Northern North Sea. a) Time series of wind speed and direction (sticks) and wind speed (bold line) corrected to 10 m height; b) Bulk shear squared; c) Direction of bulk shear (dots) compared to rotation at local inertial frequency (lines). Bulk shear squared and bulk shear direction have been filtered with a box filter of 2 h length. 29

4 Bulk properties at the station NNS during days 288 (Oct 16) to 298 (Oct 26) in 1998; a) absolute value of surface wind stress, $|\tau_s|$; b) bulk shear squared, S^2; c) time derivative of the bulk shear squared, $\partial_t S^2$, and production of bulk shear squared, $P\left(S^2\right)$, according to equation (11). $\partial_t S^2$ and $P\left(S^2\right)$ have both been first computed from instantaneous ADCP data and filtered afterwards; d) direction of surface shear stress and bulk shear. Circles denote time of alignment between bulk shear and wind direction for $S^2 > 2 \cdot 10^{-5}\mathrm{s}^{-2}$. S^2 and $P\left(S^2\right)$ have been filtered with a box filter of 2 h length, $\partial_t S^2$ has been filtered with a box filter of 4 h length. 30

5 The role of bed stress for the generation of bulk shear squared: a) bed stress, τ_b, calculated from u_b and v_b; b) bed stress direction calculated from u_b and v_b (line), overlaid with bulk shear direction (dots); c) surface stress and bed stress contributions to the total generation of bulk shear squared, P_s, P_b, respectively. All time series have been filtered with a box filter of 2 h length. 31

6 Barotropic contribution to bulk shear: a) contributions of barotropic flow, P_m, and bed dissipation, D_b, to bulk shear loss due to bed stress. b) depth-mean flow direction (line), overlaid with bulk shear direction (dots); All time series have been filtered with a box filter of 2 h length. 32

7 Time series of bulk shear squared, S^2, compared to the interfacial shear squared, S_i^2, both having been filtered with a box filter of 2 h length. Note the factor of 50 difference in scales. 33

8 Comparison between bulk shear (panels a and b) with dissipation rate (panels a and c) and eddy diffusivity (panels b and d) averaged over the thermocline. Each data point represents averages over one burst sample. The observations for dissipation rates and eddy diffusivity are from the MST (open circles) and the FLY (bullets) velocity micro-structure profilers. See Prandke et al. (2000) for the MST details and Rippeth et al. (2003) for the FLY details. The horizontal bold lines indicate the averages of dissipation rate and eddy diffusivity calculated from the MST profiles for the two 2.5 day evaluation periods compared in table 1. 34

9 Two-layer model sensitivity study with a clockwise tide and a Gaussian eastward wind burst centred at $t/T = 5$ with 20 m/s wind velocity and duration of 1 tidal period (see upper two panels). Shown are for an initial tidal phase of 270° the bulk shear squared, S^2 (middle left), the production of bulk shear squared due to wind stress, P_s, and due to depth-mean current, P_m (middle right), the phase angle of the shear and the tide, lower left, and the dissipation of bulk shear squared due to interfacial and bottom friction, $-D_i$, and $-D_b$, respectively. Results are shown for a periodical steady state. 35

10 Same as figure 9, but for an initial tidal phase of 90°. 36

11 Two-layer model sensitivity study with a Gaussian eastward wind burst centred at $t/T = 5$ with 20 m/s wind velocity and duration of 1 tidal period (see upper panels). Shown are the shear squared, S^2 (thin lines), and the wind forcing, P_s (bold lines). Simulations were carried out periodically at a period of 10 tidal periods with the wind burst repeating each 10th tide. Results are shown for a periodical steady state. The character of the tide with a tidal velocity amplitude of 0.3 m/s was varied between clockwise (left), rectilinear (centre) and anti-clockwise (right). The initial tidal phase was varied by steps of 90 ° (rows). . . 37

12 Same as figure 11, but with a wind burst duration of 3 tidal periods. 38

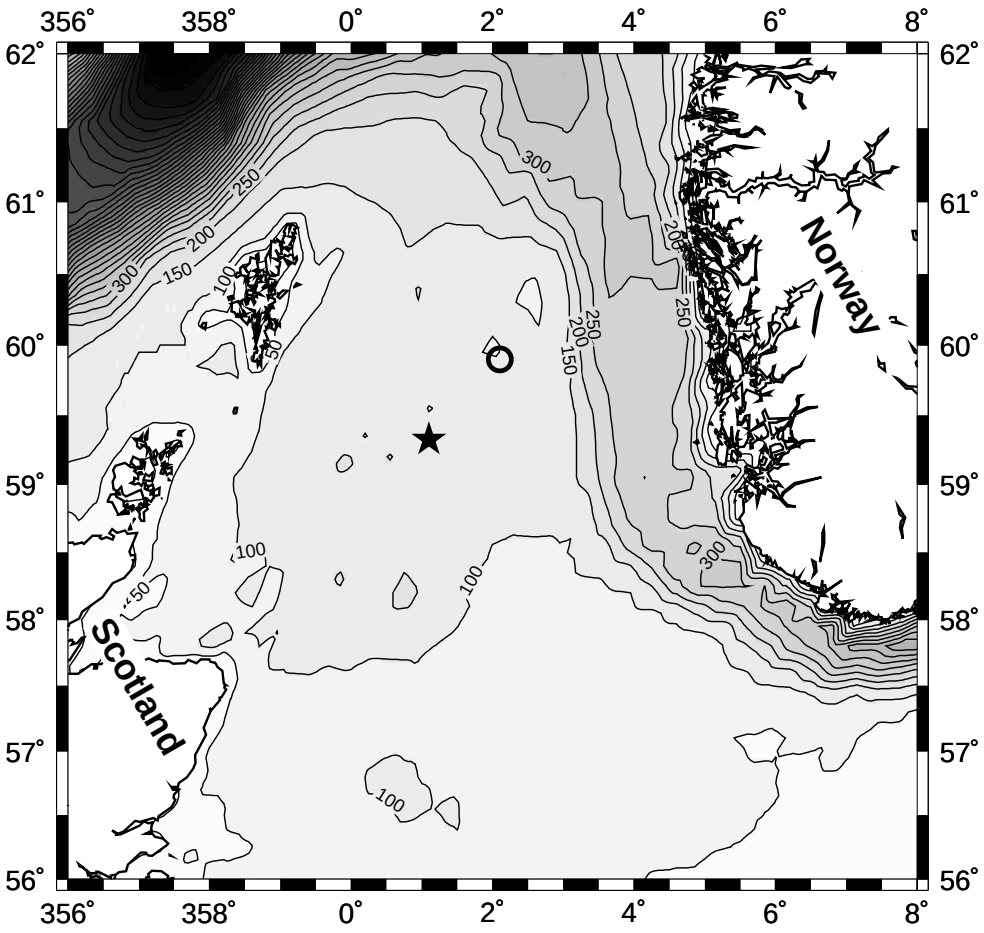

FIG. 1. Location of the PROVESS station A in the Northern North Sea (at 59°20'N and 1°E, marked by a star) at a water depth of 110 m. The location of the Frigg oil rig where meteorological parameters have been observed is marked by a circle (at 59°54'N and 2°6'E). Contour lines and shading show the water depth, the contour interval is 50 m.

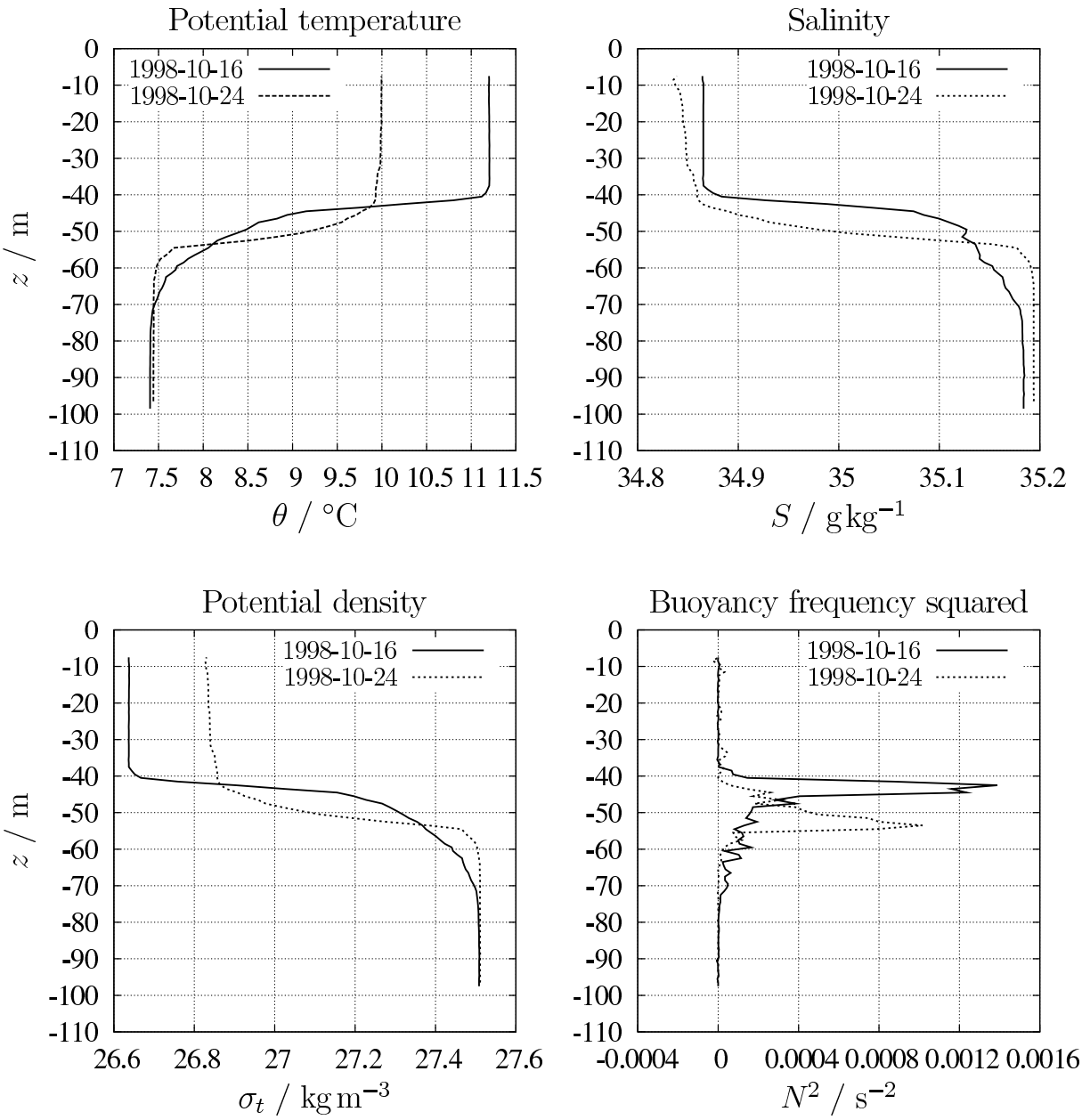

FIG. 2. Observed profiles of potential temperature, salinity, potential density and buoyancy frequency squared at the beginning (16 October 1998, 7:03 h) and one day before the end (24 October 1998, 17:04 h) of the investigated 10-day period.

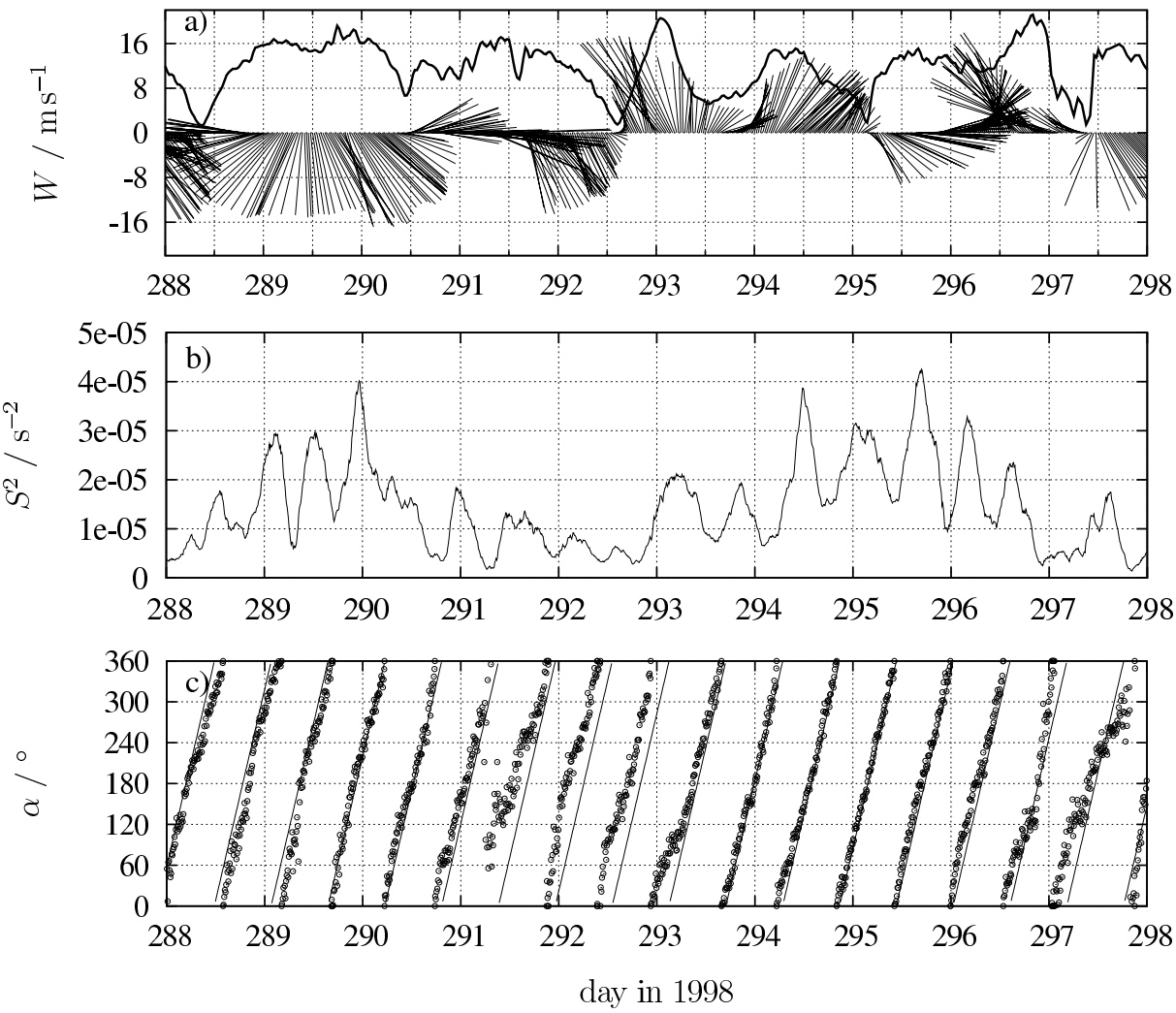

FIG. 3. Observations of wind and bulk shear vector in the Northern North Sea. a) Time series of wind speed and direction (sticks) and wind speed (bold line) corrected to 10 m height; b) Bulk shear squared; c) Direction of bulk shear (dots) compared to rotation at local inertial frequency (lines). Bulk shear squared and bulk shear direction have been filtered with a box filter of 2 h length.

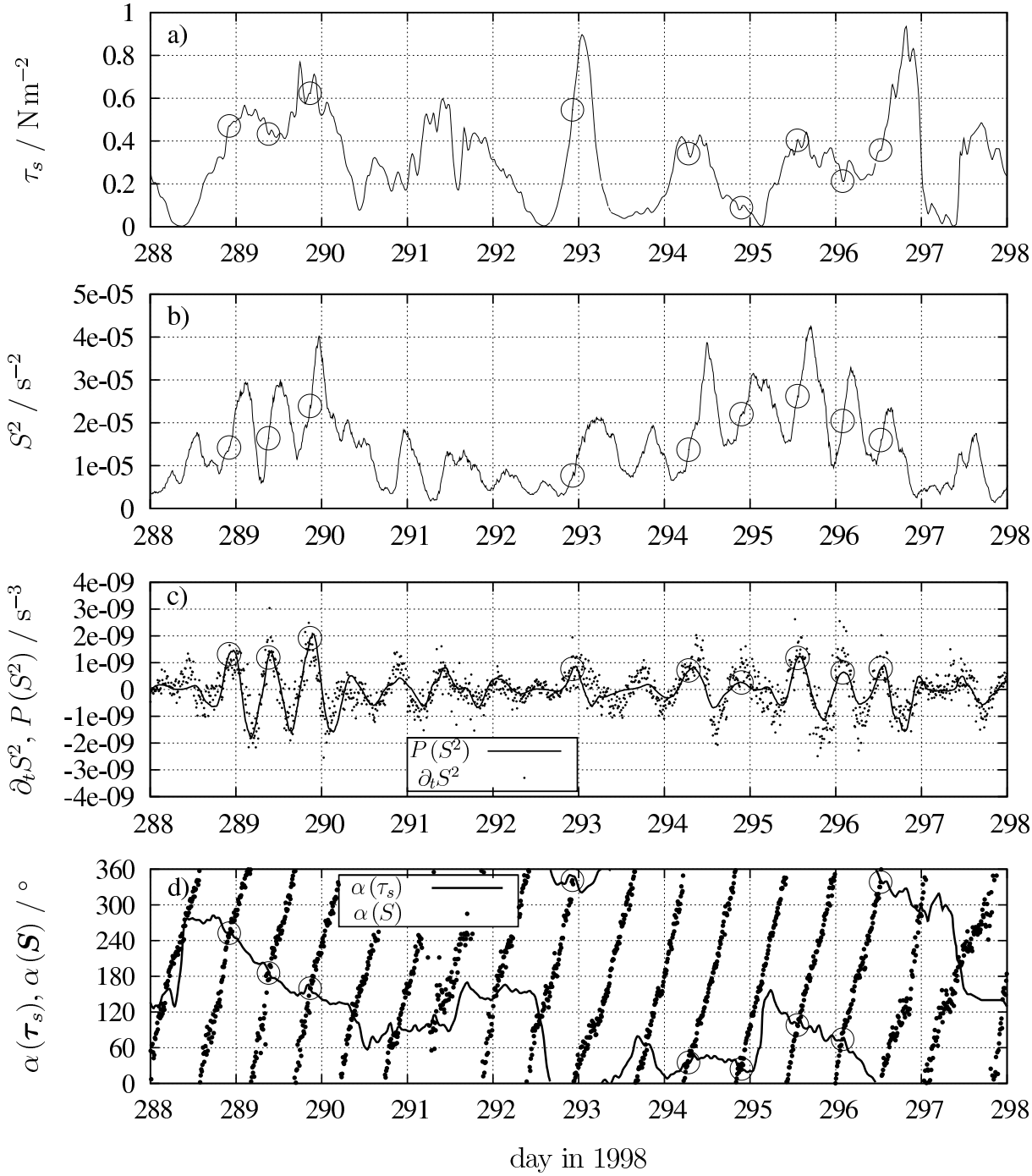

FIG. 4. Bulk properties at the station NNS during days 288 (Oct 16) to 298 (Oct 26) in 1998; a) absolute value of surface wind stress, $|\tau_s|$; b) bulk shear squared, S^2; c) time derivative of the bulk shear squared, $\partial_t S^2$, and production of bulk shear squared, $P(S^2)$, according to equation (11). $\partial_t S^2$ and $P(S^2)$ have both been first computed from instantaneous ADCP data and filtered afterwards; d) direction of surface shear stress and bulk shear. Circles denote time of alignment between bulk shear and wind direction for $S^2 > 2 \cdot 10^{-5}\mathrm{s}^{-2}$. S^2 and $P(S^2)$ have been filtered with a box filter of 2 h length, $\partial_t S^2$ has been filtered with a box filter of 4 h length.

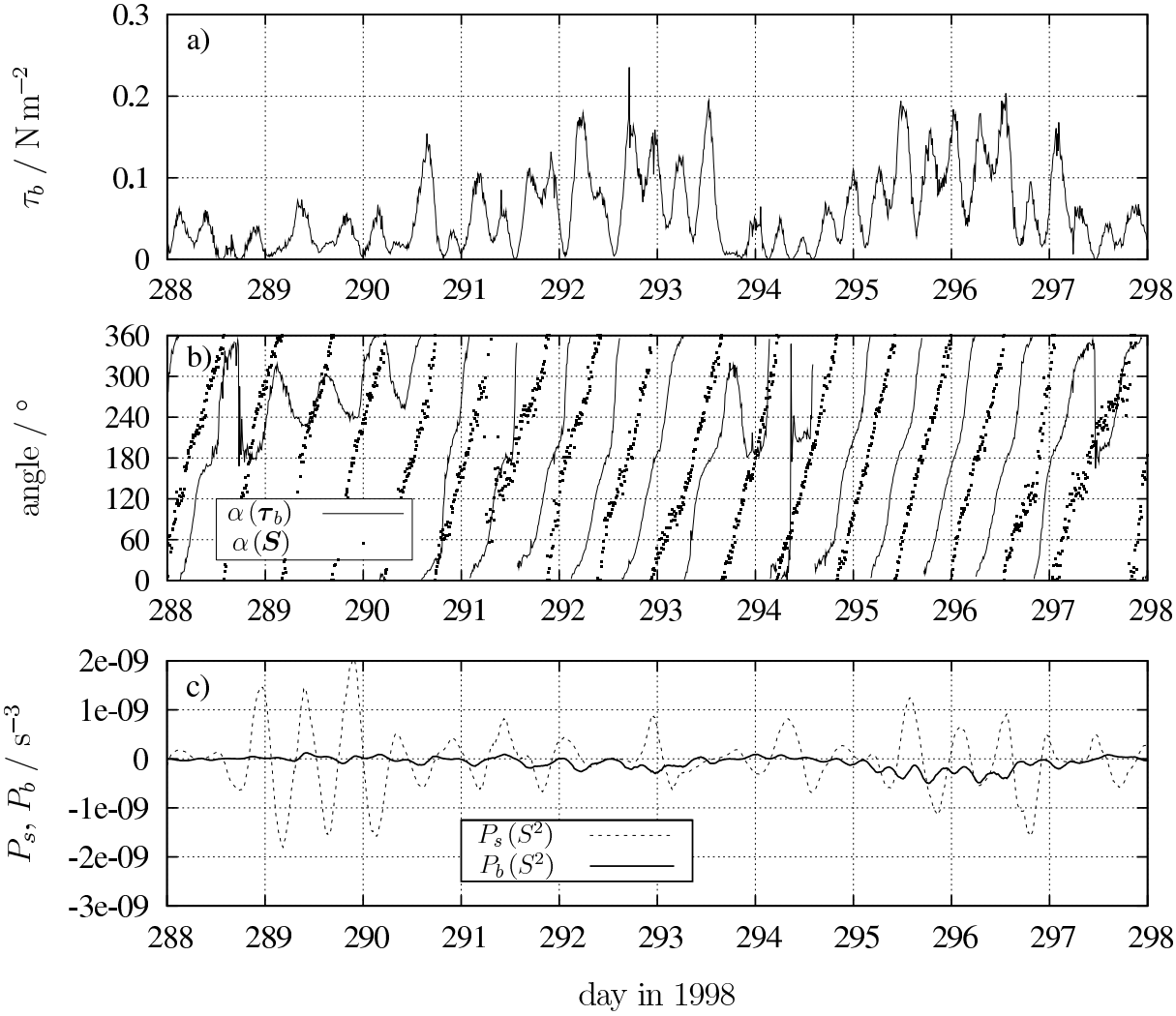

FIG. 5. The role of bed stress for the generation of bulk shear squared: a) bed stress, τ_b, calculated from u_b and v_b; b) bed stress direction calculated from u_b and v_b (line), overlaid with bulk shear direction (dots); c) surface stress and bed stress contributions to the total generation of bulk shear squared, P_s, P_b, respectively. All time series have been filtered with a box filter of 2 h length.

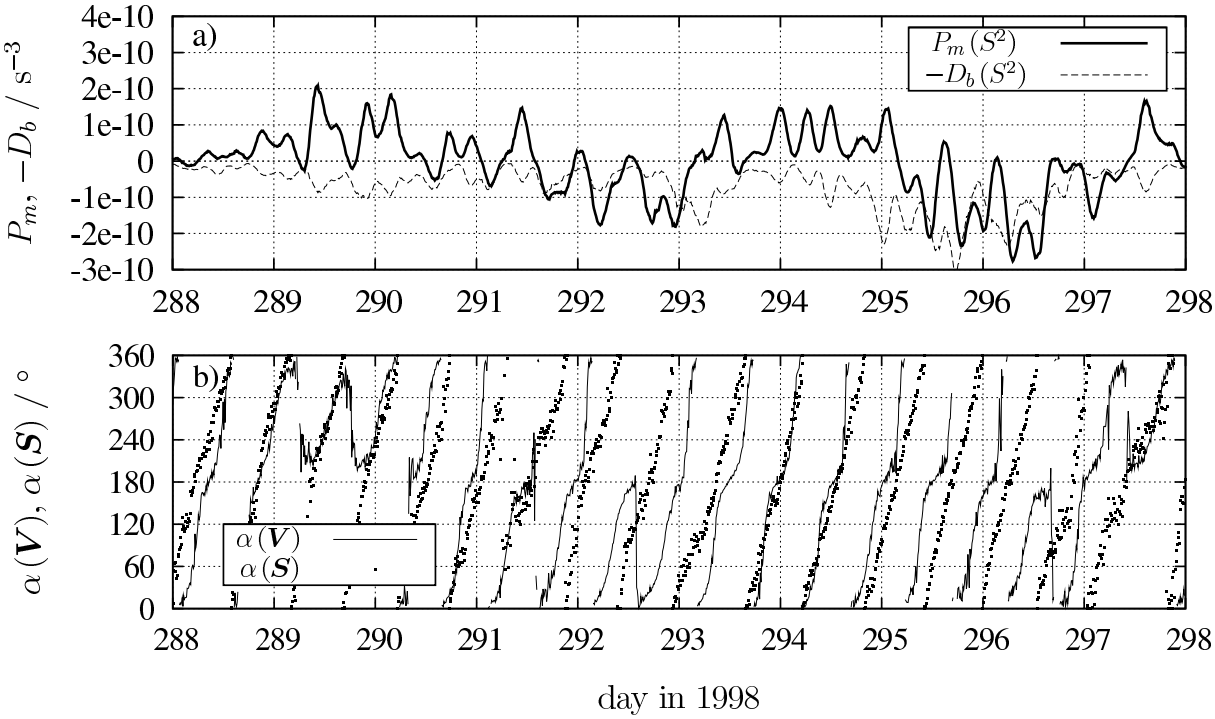

FIG. 6. Barotropic contribution to bulk shear: a) contributions of barotropic flow, P_m, and bed dissipation, D_b, to bulk shear loss due to bed stress. b) depth-mean flow direction (line), overlaid with bulk shear direction (dots); All time series have been filtered with a box filter of 2 h length.

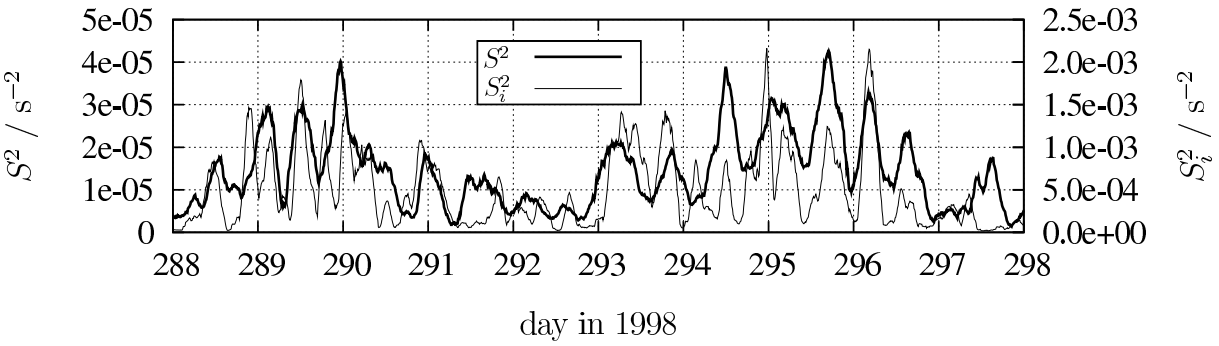

FIG. 7. Time series of bulk shear squared, S^2, compared to the interfacial shear squared, S_i^2, both having been filtered with a box filter of 2 h length. Note the factor of 50 difference in scales.

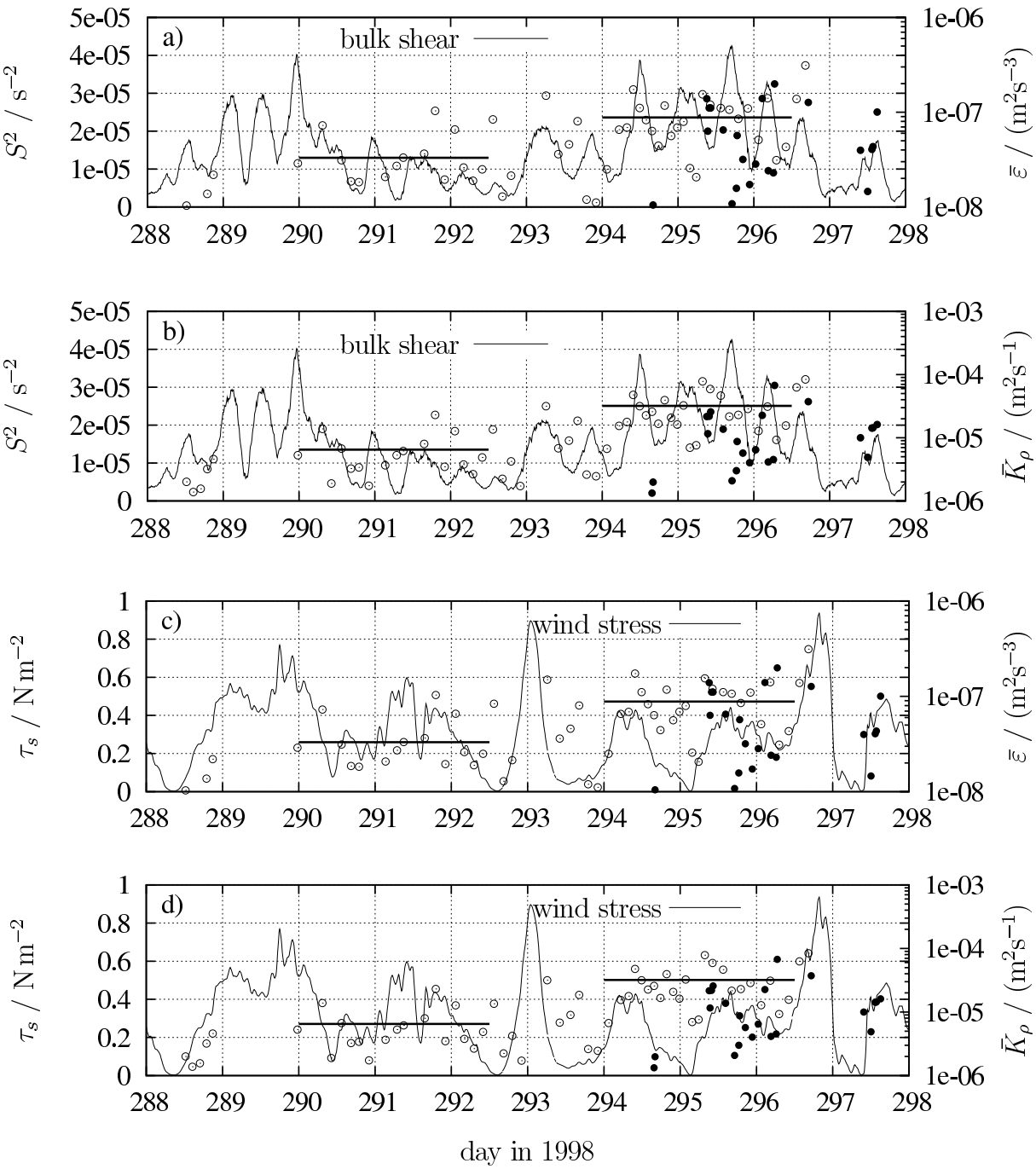

FIG. 8. Comparison between bulk shear (panels a and b) with dissipation rate (panels a and c) and eddy diffusivity (panels b and d) averaged over the thermocline. Each data point represents averages over one burst sample. The observations for dissipation rates and eddy diffusivity are from the MST (open circles) and the FLY (bullets) velocity micro-structure profilers. See Prandke et al. (2000) for the MST details and Rippeth et al. (2003) for the FLY details. The horizontal bold lines indicate the averages of dissipation rate and eddy diffusivity calculated from the MST profiles for the two 2.5 day evaluation periods compared in table 1.

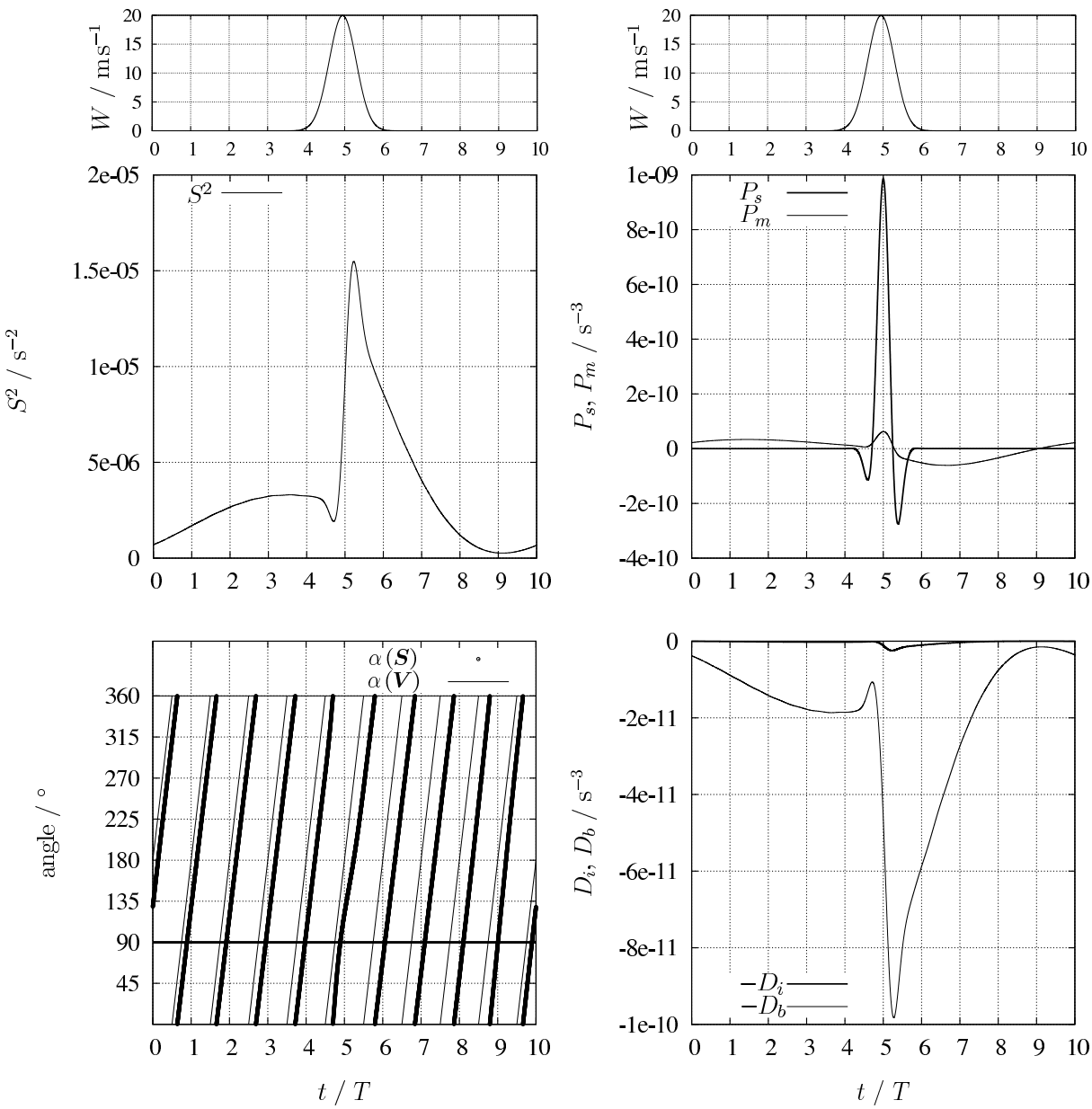

FIG. 9. Two-layer model sensitivity study with a clockwise tide and a Gaussian eastward wind burst centred at $t/T = 5$ with 20 m/s wind velocity and duration of 1 tidal period (see upper two panels). Shown are for an initial tidal phase of 270° the bulk shear squared, S^2 (middle left), the production of bulk shear squared due to wind stress, P_s, and due to depth-mean current, P_m (middle right), the phase angle of the shear and the tide, lower left, and the dissipation of bulk shear squared due to interfacial and bottom friction, $-D_i$, and $-D_b$, respectively. Results are shown for a periodical steady state.

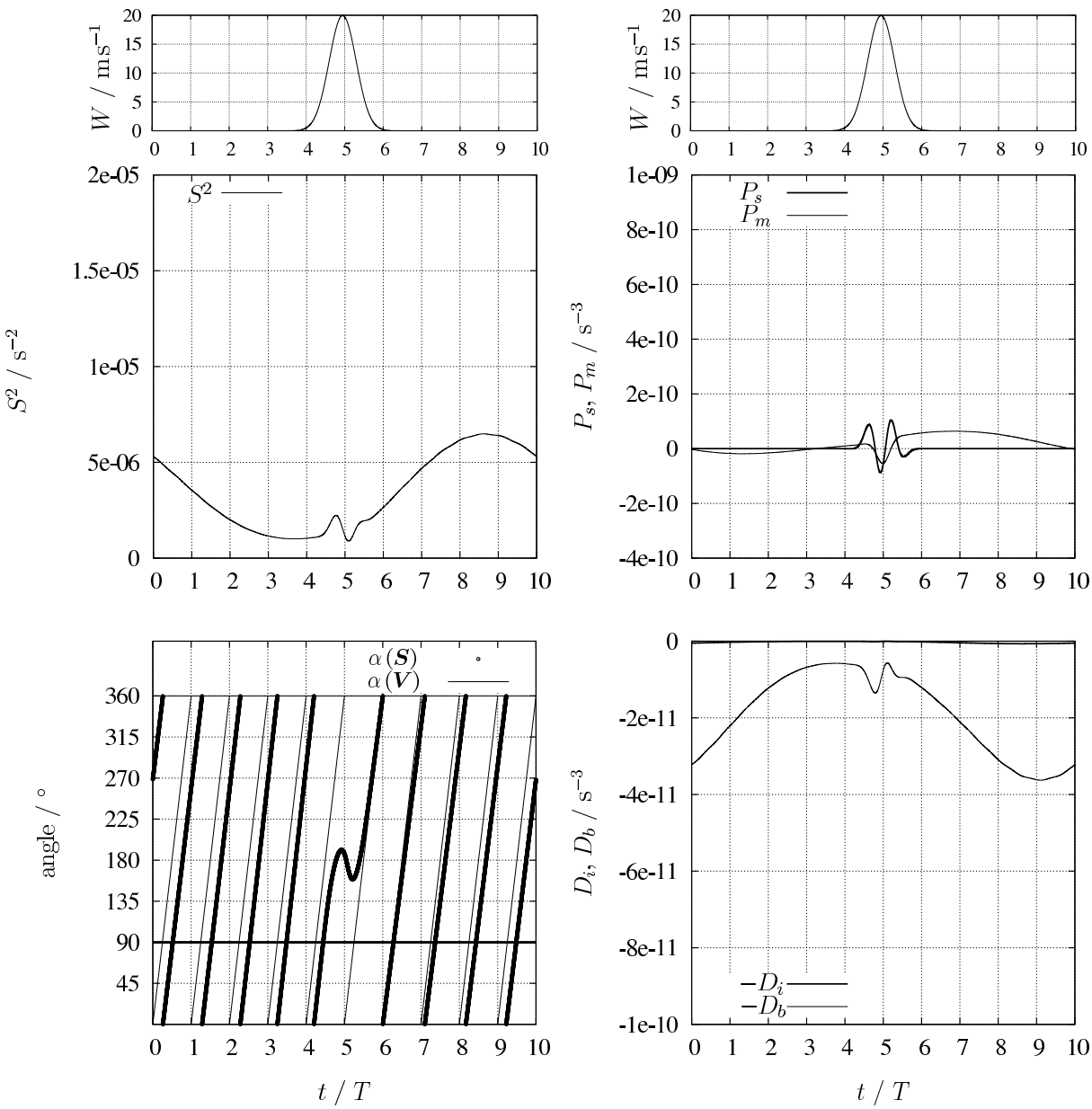

FIG. 10. Same as figure 9, but for an initial tidal phase of 90°.

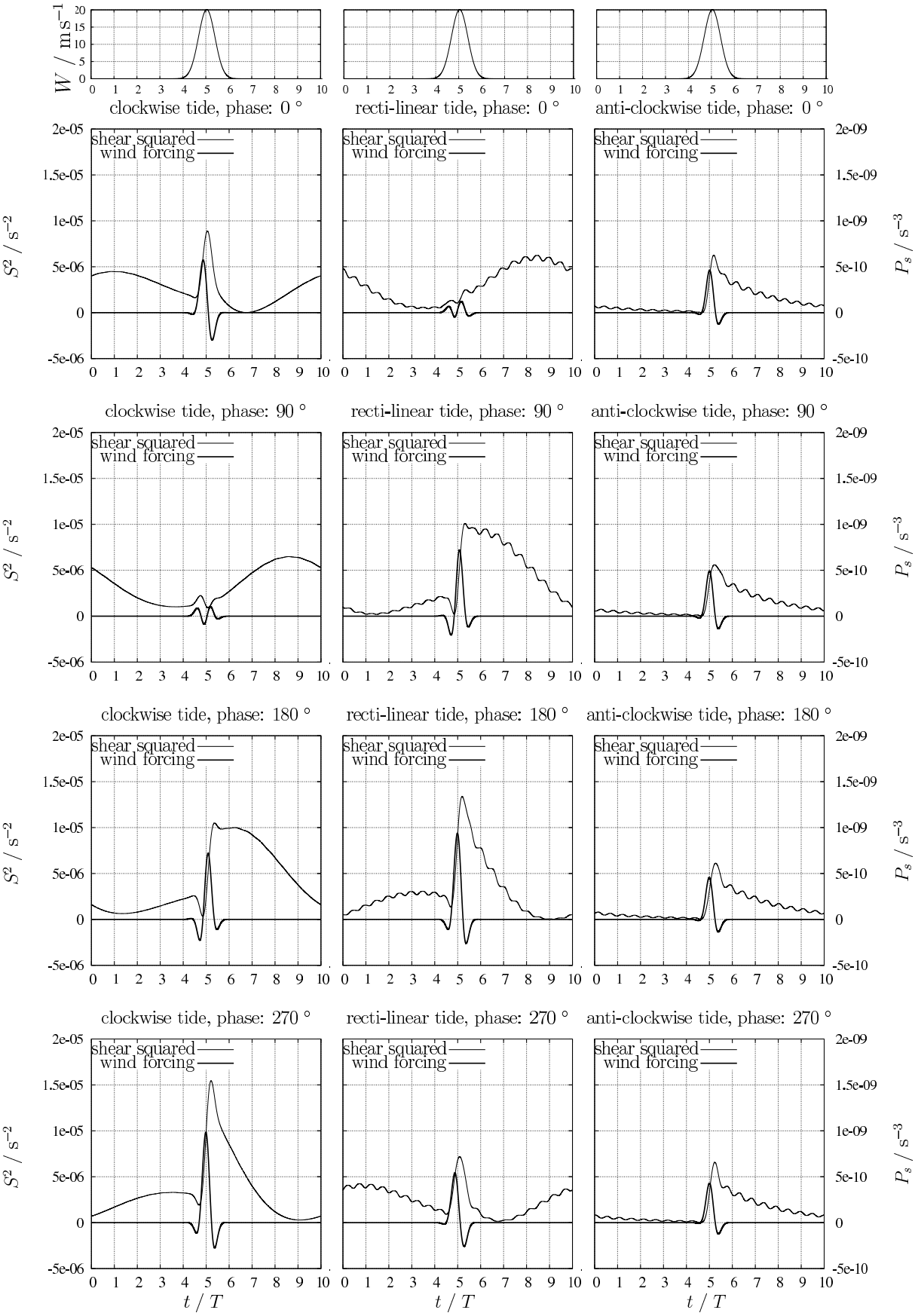

FIG. 11. Two-layer model sensitivity study with a Gaussian eastward wind burst centred at $t/T = 5$ with 20 m/s wind velocity and duration of 1 tidal period (see upper panels). Shown are the shear squared, S^2 (thin lines), and the wind forcing, P_s (bold lines). Simulations were

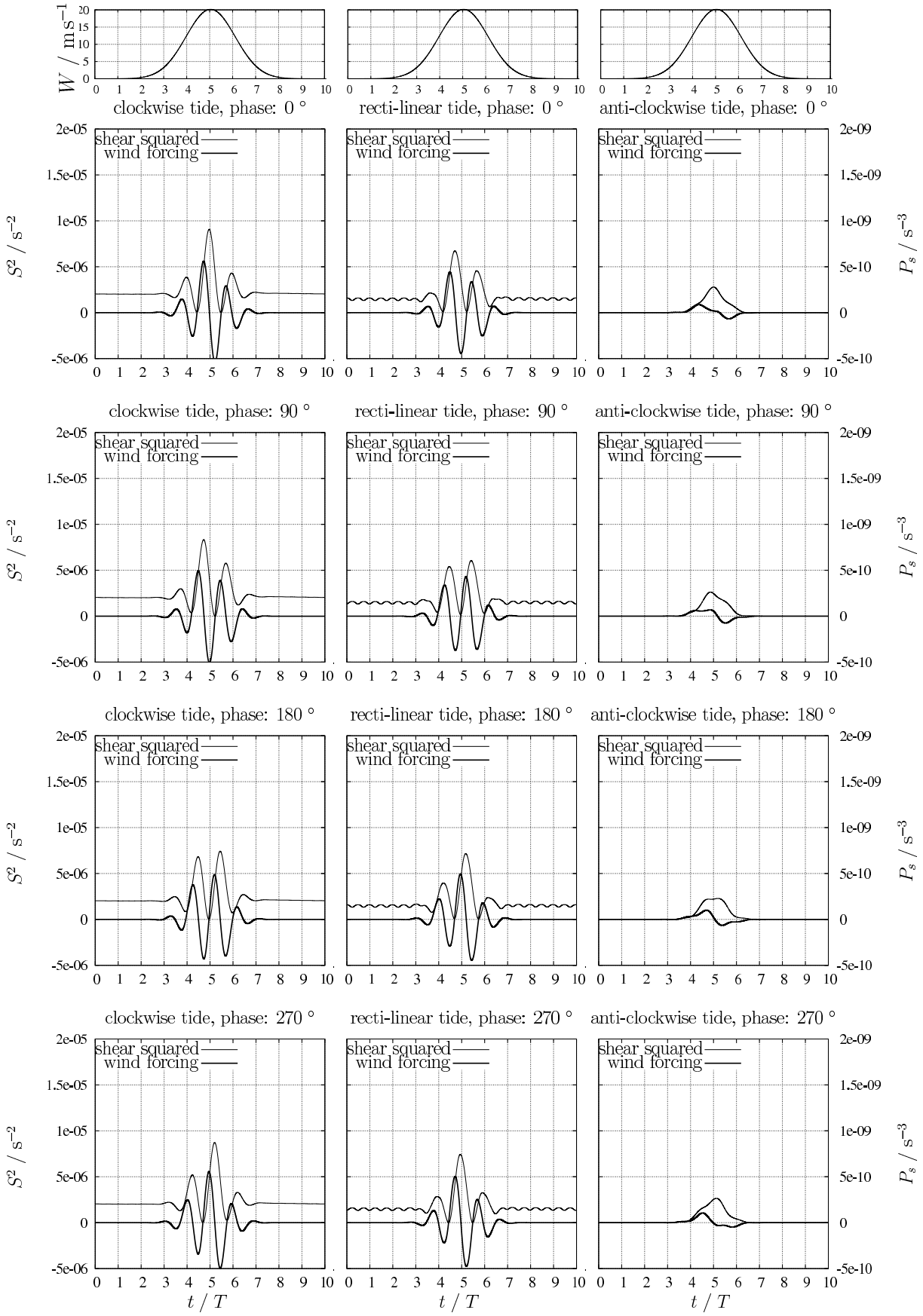

FIG. 12. Same as figure 11, but with a wind burst duration of 3 tidal periods.

List of Tables

1 Average values of bulk shear cubed, S^3, surface wind stress to the power of 3/2, $(\tau^s)^{3/2}$, dissipation rate, ε, and eddy diffusivity K_ρ, for two periods of comparable wind strength and different bulk shear. The latter two quantities have been derived from MST micro-structure profiler data only. The 95% confidence intervals which have been calculated using the bootstrap method are given in brackets. 40

	ave$\{S^3\}$	ave$\left\{(\tau^s)^{3/2}\right\}$	ave$\{\bar{\varepsilon}\}$	ave$\left\{\bar{K}_\rho\right\}$
Days 290.0 - 292.5	$3.8 \cdot 10^{-8}$s^{-3}	0.19 (N m^{-2})$^{3/2}$	$3.3 \cdot 10^{-8}$ W kg ($2.8 \cdot 10^{-8}$ W kg ... ... $3.8 \cdot 10^{-8}$ W kg)	$6.5 \cdot 10^{-6}$ m^{2}s^{-1} ($5.5 \cdot 10^{-6}$ m^{2}s^{-1} ... ... $7.6 \cdot 10^{-6}$ m^{2}s^{-1})
Days 294.0 - 296.5	$1.1 \cdot 10^{-7}$s^{-3}	0.14 (N m^{-2})$^{3/2}$	$8.8 \cdot 10^{-8}$ W kg ($7.8 \cdot 10^{-8}$ W kg ... ... $10.1 \cdot 10^{-8}$ W kg)	$3.2 \cdot 10^{-5}$ m^{2}s^{-1} ($2.7 \cdot 10^{-5}$ m^{2}s^{-1}... ... $3.6 \cdot 10^{-5}$ m^{2}s^{-1})

TABLE 1. Average values of bulk shear cubed, S^3, surface wind stress to the power of 3/2, $(\tau^s)^{3/2}$, dissipation rate, ε, and eddy diffusivity K_ρ, for two periods of comparable wind strength and different bulk shear. The latter two quantities have been derived from MST micro-structure profiler data only. The 95% confidence intervals which have been calculated using the bootstrap method are given in brackets.